PAPER

Check for updates

Microwave-synthesized Bi_2MoO_6 nanoplates for high performance symmetric and asymmetric supercapattery devices†

Anu,[a] Pawanpreet Kour,[a] Khadim Hussain,[b] Prakash Chand,[c] J. Nagendra Babu,[b] C. S. Yadav,[d] Joel Garcia, ID *[e] Surender Kumar Sharma*[a] and Kamlesh Yadav ID *[f]

Here, we explore the potential of symmetric and asymmetric configurations for high-performance energy storage using Bi_2MoO_6 (BMO) nanoplates synthesized *via* a microwave-hydrothermal method. Symmetric devices (BMO//BMO) exhibit a higher specific capacity ($\sim$83 mAh g^{-1}), but lower retention ($\sim$36% after 1250 cycles), while asymmetric devices (BMO//carbon nanotubes (CNTs)) show superior retention ($\sim$85% after 2500 cycles) with a capacity of $\sim$46.25 mAh g^{-1}. The enhanced redox activity in symmetric format contrasts with the conductive benefits of CNTs in asymmetric systems. This dual evaluation demonstrates the versatility of BMO for both energy density and long-term stability, making it a promising material for high-performance energy storage applications. Furthermore, we provide a detailed analysis of the charge storage mechanism of BMO, which follows a battery-type process driven by intercalation and redox reactions, resulting in its high capacity. The practicality of the BMO//BMO device is demonstrated by lighting red, green, and blue LEDs for 18 minutes, 45 seconds, and 30 seconds, respectively, using two identical supercapacitor cells connected in series.

1. Introduction

Batteries and supercapacitors are well-known energy storage devices, each with unique advantages and limitations. Batteries can store a significant amount of energy for long periods. However, their power density is relatively low, and they charge and discharge at a slower rate. On the other hand, supercapacitors offer high power density, enabling rapid charging and discharging, but they are limited by low energy density, which restricts their storage capacity. Supercapatteries address these limitations by achieving an optimal balance: they provide higher energy density than supercapacitors, ensuring a longer discharge time, and exhibit a greater power density than

batteries, allowing faster energy access when needed. This dual functionality makes supercapatteries ideal for applications that demand both quick bursts of power and moderate energy storage, such as in electric vehicles, renewable energy storage, and grid stabilization systems. Their ability to offer both rapid charging and extended operation times highlights their significance as next-generation energy storage devices that are designed to meet the growing demands for efficiency and versatility.[1–4] Various metal oxides, such as Co_3O_4,[5] TiO_2,[6] CeO_2,[7] Bi_2O_3,[8] $CeNiO_3$,[9] $BiFeO_3$,[10] $MnCo_2O_4$,[11] $Bi_4Ti_3O_{12}$,[12] Bi_2WO_6,[13] and Bi_2MoO_6,[14,15] have been investigated for use in supercapattery devices. Among these, Aurivillius-type compounds like $Bi_4Ti_3O_{12}$, Bi_2WO_6, and Bi_2MoO_6, have gained attention as promising candidates due to their distinctive structural and electrochemical properties. The layered structure of these materials facilitates ion diffusion and electron transport – key factors in enhancing electrochemical performance. Additionally, their 2D morphology offers a large surface area, promoting efficient ion adsorption and improving access to electrochemically active sites. Despite these advantages, several challenges remain in the use of 2D layered metal oxides for supercapattery applications. These challenges include structural instability during prolonged cycling, low intrinsic conductivity in some metal oxides, and limited scalability of the synthesis methods.[4,11–16] Compared to Aurivillius-type layered structure $Bi_4Ti_3O_{12}$ and Bi_2WO_6, Bi_2MoO_6 (BMO) demonstrates

[a] *Department of Physics, School of Basic Sciences, Central University of Punjab, Bathinda, 151401, Punjab, India. E-mail: surender.sharma@cup.edu.in*

[b] *Department of Chemistry, School of Basic Sciences, Central University of Punjab, Bathinda, 151401, Punjab, India*

[c] *Department of Physics, National Institute of Technology, Kurukshetra, 136119, India*

[d] *School of Basic Sciences, Indian Institute of Technology Mandi, Mandi, 175005, Himachal Pradesh, India*

[e] *Department of Chemistry, De La Salle University, Manila, Philippines. E-mail: joel.garcia@dlsu.edu.ph*

[f] *Department of Physics, University of Allahabad, Prayagraj, 211002, Uttar Pradesh, India. E-mail: kamleshyadav@allduniv.ac.in*

† Electronic supplementary information (ESI) available. See DOI: https://doi.org/10.1039/d5ma00647c

superior electrochemical performance in supercapattery applications. This is primarily attributed to its superior intrinsic faradaic activity and improved cycling stability, making it an excellent choice for applications demanding both high power and energy density.[12,14,15,17,18]

BMO is an intriguing compound that belongs to the Aurivillius family of oxides, known for their layered perovskite structures. This material has gained attention due to its unique photocatalytic, dielectric, and electrochemical properties.[19,20] In recent years, BMO has been explored for various energy storage and conversion applications, including its potential use in supercapattery devices.[14,15,21–28] In BMO, bismuth oxide layers alternate with molybdate octahedra (MoO_6).[29] This arrangement creates a natural two-dimensional framework that facilitates ion diffusion and electron transport, which are crucial for its electrochemical performance. BMO can participate in faradaic reactions, enabling the material to act as a battery-like electrode in supercapatteries.[18,21] The layered structure of BMO offers a high surface area for ion adsorption and electrostatic charge storage, similar to the behaviour seen in supercapacitors. This capacitive component enhances the power density of the material, allowing for rapid charge/discharge cycles. The combination of faradaic and capacitive behaviours in BMO results in a hybrid energy storage mechanism, which is the hallmark of supercapattery devices. This hybrid mechanism allows BMO to strike a balance between energy density, similar to batteries, and power density, like supercapacitors.

Most studies in this field have concentrated on the synthesis and characterization of BMO nanostructures, followed by the evaluation of their electrochemical performance in a three-electrode system. Previous studies predominantly relied on traditional synthesis methods, such as solvothermal techniques, which often result in longer processing times, lower reproducibility, and limited control over nanostructure morphology. These limitations present significant challenges, potentially impeding the full exploitation of BMO's electrochemical capabilities. Notably, the adoption of microwave-assisted hydrothermal methods has emerged as a superior alternative. This innovative technique offers several advantages, including rapid synthesis, improved uniformity, and greater control over nanostructure formation. Microwave-assisted hydrothermal synthesis enables a more efficient and consistent production process, significantly improving the electrochemical performance of BMO and enhancing its viability for advanced energy storage applications. In several studies, BMO has been observed to exhibit battery-like behavior, characterized by distinct redox peaks when tested in alkaline electrolytes such as KOH and NaOH. This suggests that the material behaves more like a battery electrode, with its capacity governed by redox reactions occurring at the electrode surface. Despite this, many reports mistakenly calculate the specific capacitance (F g^{-1}) instead of the specific capacity (mAh g^{-1}) when evaluating its electrochemical performance.[14,15,21–28,30,31] This practice can lead to misleading conclusions, as specific capacitance is more appropriate for materials that store charge primarily through electrostatic means (as in electrical double-layer

capacitors), rather than those that involve faradaic processes. Calculating specific capacitance for BMO, which relies on redox reactions, fails to capture the true extent of its charge storage capabilities and may undervalue its performance in applications where battery-like behavior is desirable. Therefore, a more accurate assessment of BMO's electrochemical properties should involve calculating the specific capacity. This reflects its battery-like behavior and enhances the understanding of its suitability for energy storage applications. In addition to three-electrode systems, recent studies have extended the investigation of BMO's electrochemical properties to symmetric supercapacitor configurations.[14,15,18] Samdani et al. (2018) fabricated a carbon sphere@BMO symmetric supercapattery device using a thin film of PVA-KOH as both the separator and electrolyte. This device achieved a specific capacitance of 26.69 F g^{-1} at 0.25 A g^{-1}, an energy density of 10.8 Wh kg^{-1} at a power density of 410 W kg^{-1}, and maintained 80% of its specific capacitance after 10 000 cycles.[15] Likewise, Shinde et al. (2019) developed a BMO symmetric supercapattery device incorporating a polypropylene separator and a 1 M KOH electrolyte. The device achieved a specific capacitance of 40.5 F g^{-1} at 1 A g^{-1}, and an energy density of 45.6 Wh kg^{-1} at a power density of 989 W kg^{-1}, and it retained 78% of its capacitance after 5000 cycles.[14] Wang et al. (2020) expanded on this research by fabricating BMO quasi-nanospheres anchored onto activated carbon cloth for flexible symmetric devices, utilizing a PVA-KOH gel electrolyte. Their device exhibited a specific capacitance of 345.0 F g^{-1} at 1 A g^{-1}, an energy density of 110.4 Wh kg^{-1} at a power density of 1429.6 W kg^{-1}, and retained 90.2% of its capacitance after 10 000 cycles.[18]

While these studies have significantly advanced our understanding of BMO as a supercapacitor material, several gaps remain. Many of these investigations have relied on traditional synthesis methods, such as solvothermal techniques, which are often hampered by longer processing times and limited control over nanostructure morphology. Furthermore, a significant number of studies are confined to three-electrode systems, which do not provide a comprehensive view of the material's performance in practical applications. Most importantly, the performance of BMO in asymmetric devices has yet to be explored, and systematic comparisons between symmetric and asymmetric configurations are lacking. Addressing these gaps, the present study aims to advance the understanding and application of BMO in supercapattery devices by employing a novel microwave-assisted hydrothermal synthesis method. Additionally, this research will evaluate the electrochemical performance of BMO not only in three-electrode systems but also in both symmetric and asymmetric supercapattery configurations. In a departure from previous studies, we calculated specific capacity (mAh g^{-1}) instead of specific capacitance (F g^{-1}) for BMO, aligning with its battery-like behavior to yield a more accurate assessment of its electrochemical performance. This approach provides deeper insight into BMO's charge storage mechanism, which operates through faradaic processes, highlighting its potential as a promising battery-type material for energy storage. Furthermore, by incorporating

carbon nanotubes (CNTs) as the complementary electrode material in asymmetric devices, this study aims to enhance overall device performance and provide a more thorough evaluation of BMO's practical potential. Finally, our research aspires to provide important insights into the development of high-performance supercapattery device design and optimization, assisting in the creation of efficient and adaptable next-generation energy storage systems.

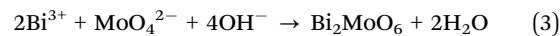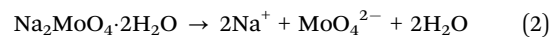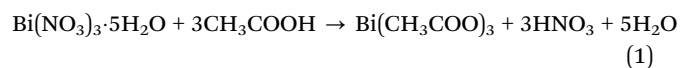the adopted synthesis conditions, and can be divided into the following main stages: (a) dissolution and hydrolysis, (b) nucleation, (c) aggregation, and (d) crystallization:[14,32]

$$Bi(NO_3)_3 \cdot 5H_2O + 3CH_3COOH \rightarrow Bi(CH_3COO)_3 + 3HNO_3 + 5H_2O \tag{1}$$

$$Na_2MoO_4 \cdot 2H_2O \rightarrow 2Na^+ + MoO_4^{2-} + 2H_2O \tag{2}$$

$$2Bi^{3+} + MoO_4^{2-} + 4OH^- \rightarrow Bi_2MoO_6 + 2H_2O \tag{3}$$

2. Experimental section

2.1. Materials and chemicals

Bismuth(III) nitrate pentahydrate [$Bi(NO_3)_3 \cdot 5H_2O$, Aldrich, $\geq 98\%$] and sodium molybdate, dihydrate [$Na_2MoO_4 \cdot 2H_2O$, Aldrich, $\geq 99\%$], concentrated HNO_3 (Loba, 69%), super-P carbon black, polyvinylidene fluoride (PVDF), N-methylpyrrolidone (NMP), and double distilled water (DDW) were used.

2.2. Preparation of BMO

Specifically, 0.05 M of $Bi(NO_3)_3 \cdot 5H_2O$ was dissolved in 10 ml of glacial acetic acid to obtain a clear and transparent solution, to which 0.025 M of $Na_2MoO_4 \cdot 2H_2O$ was added and stirred thoroughly. The volume of the resulting solution was adjusted to 50 mL using DDW, and a few drops of NH_3 were added to reach a final pH of approximately 8.0. The solution was then subjected to MW treatment at 180 °C for 30 minutes in an 80 mL glass vial, filled to 60% capacity. Following MW treatment, pale yellow precipitates formed and were subsequently washed with DDW and ethanol through centrifugation. The washed precipitates were dried at 60 °C for 24 hours in a vacuum oven and subjected to further characterizations. Fig. 1 showcases a pictorial diagram illustrating the synthesis process of BMO NPs. The following reactions (1)–(3) are proposed based on

2.3. Material characterizations

X-ray diffraction (XRD) was used to examine the materials' purity and the phase structure of the materials. A NEXSA surface analysis XPS spectrometer from thermo scientific was used to perform X-ray photoelectron spectroscopy (XPS). The Raman spectra were obtained at room temperature using a Horiba Lab RAM HR evolution mode Raman spectrometer. An FESEM, 6 Merlin compact 6073, and Carl Zeiss were used to characterize the surface morphology. An energy-dispersive X-ray analyzer (EDX) in conjunction with the FESEM device verified the elemental makeup of the produced samples. A Bruker Tensor 27 FTIR spectrometer was used to record the transmission spectrum of Fourier-transform infrared spectroscopy (FTIR) in the 600–4000 cm^{-1} range. Nitrogen adsorption–desorption isotherms were obtained using a nitrogen adsorption instrument (ASAP 2020, USA) following a 12-hour degassing process. The specific surface area was calculated using the Brunauer–Emmett–Teller (BET) method. The electrochemical characteristics were assessed with an (CHI 760E, USA) electrochemical analyzer in both three-electrode and two-electrode setups.
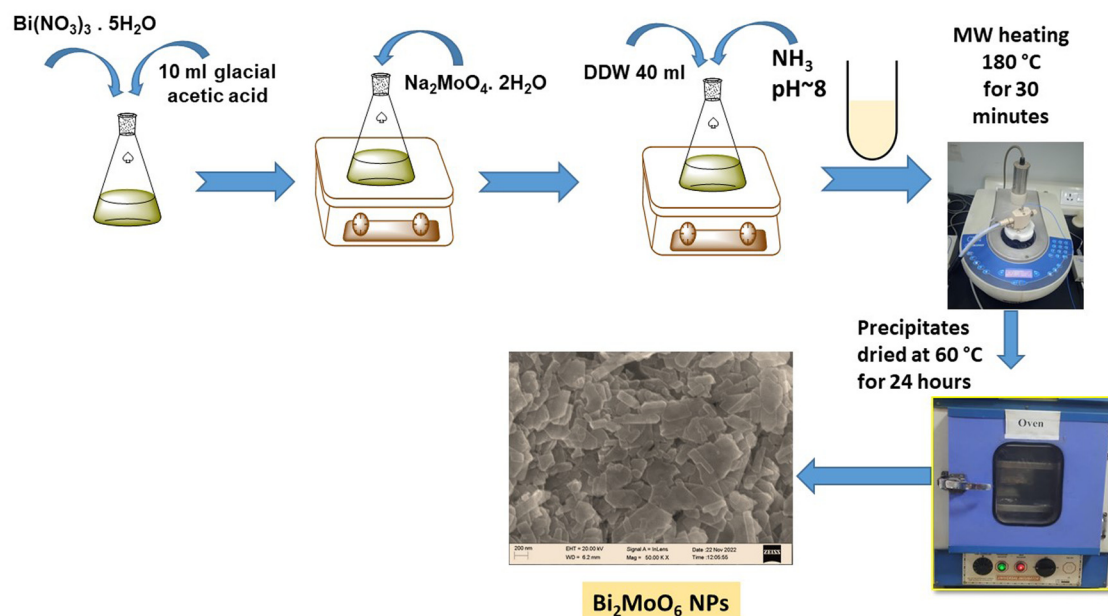

Fig. 1 Pictorial diagram showing the synthesis of Bi_2MoO_6 (BMO) NPs.

2.4. Electrochemical measurements

The CHI-760E workstation was used to evaluate the electrochemical properties of the synthesized samples in a three-electrode configuration using a 6 M KOH aqueous electrolyte at room temperature. The working electrodes were made by combining the active material (BMO), super-P carbon black, and PVDF in an 8 : 1 : 1 weight ratio. The mixture was then ultrasonically dispersed in NMP solvent to create a homogenous slurry, which was then continuously stirred for 12 hours.[12] A certain weight of the slurry was then coated onto a Ni foam substrate (10 × 10 mm, 1 mm thickness), resulting in an active material loading of roughly 0.7 mg cm^{-2}. The substrate was then allowed to dry overnight at 70 °C in a hot air oven. In the three-electrode setup, the electrochemical performance of the working electrode materials was characterized using KCl-saturated Ag/AgCl reference electrode and a platinum wire as the counter electrode. Cyclic voltammetry (CV) tests were conducted at various scan rates of 10, 20, 30, 40, 60, 80, and 100 mV s^{-1} within a potential range of 0 to 0.5 V. Additionally, galvanostatic charge/discharge (GCD) tests were performed to evaluate the charge and discharge times of all samples across different current densities. Electrochemical impedance spectroscopy (EIS) measurements were conducted over a frequency range of 0.01 Hz to 100 kHz, with a perturbation potential of 5 mV.

The specific capacity of both the single electrode and the device was determined from the CV and GCD curves using the following eqn (4) and (5):[12,33,34]

$$C_m = \frac{\int I dV}{2 \times \nu \times m} \tag{4}$$

$$C_m = \frac{2 \times I \times \int_{t_i}^{t_f} V dt}{m \times \Delta V} \tag{5}$$

where C_m represents the gravimetric specific capacity (C g^{-1}), I/m denotes the current density (A g^{-1}), ΔV is the voltage (V), ν is the scan rate (mV s^{-1}), and t_i and t_f are the initial and final discharge times, respectively.

For the asymmetric BMO//CNT, the charge balance between the positive and negative electrodes was achieved by adjusting the mass loading of the active materials in each electrode based on the following eqn (6) and (7):[11]

$$Q_+ = Q_- \tag{6}$$

$$\frac{m_+}{m_-} = \frac{C_{m_-} \times \Delta V_-}{C_{m_+} \times \Delta V_+} \tag{7}$$

Here, m$_+$ refers to the mass of the active material, and C_m signifies the specific capacity.

The Coulomb efficiency (C_E) was calculated by using the following formula as given in eqn (8):

$$C_E = \frac{t_D}{t_C} \times 100\% \tag{8}$$

where t_D is the discharge time, and t_C is the charge time.

2.5. Fabrication of the supercapattery device

We constructed two types of supercapattery devices: (i) a symmetric supercapattery (SSC) with BMO as both the positive and negative electrode (BMO//BMO) and (ii) an asymmetric supercapattery (ASC) with BMO as the positive electrode and carbon nanotubes (CNTs) as the negative electrode (BMO//CNT). The utilization of CNTs as the negative electrode in an asymmetric supercapacitor device offers numerous advantages, such as high surface area, fast ion diffusion, superior electrical conductivity, electrochemical stability, flexibility, and environmental friendliness. These characteristics make CNTs an attractive choice for enhancing the energy storage capacity, power output, and overall performance of asymmetric supercapacitors.[35,36] In both configurations, a piece of Whatman paper soaked in 6 M KOH electrolyte was used as the separator. Electrochemical analyses were performed within an optimized potential range for both the SSC and ASC setups.

The energy density (E_d) and power density (P_d) of the devices were calculated using the following eqn (9) and (10):

$$E_d = \frac{I \times \int_{t_i}^{t_f} V dt}{m} \tag{9}$$

$$P_d = \frac{3600 \times E_d}{t_D} \tag{10}$$

where C_{cell} represents the specific capacity of the device, ΔV is the operating potential, and t_D is the discharge time.

3. Results and discussion

3.1. XRD analysis

Fig. 2 presents the XRD pattern of BMO, displaying sharp and well-defined diffraction peaks consistent with the reported literature[14,15,37] and JCPDS card no. 01-076-2388, which confirms the successful formation of pure orthorhombic Bi$_2$MoO$_6$ with the Cmca space group. The peak positions and corresponding planes are well indexed. An additional peak at 17.96° belongs to the presence of minor secondary phase Bi$_2$Mo$_2$O$_9$.[38] The crystallite size (D) was determined using Scherrer's equation,[39] yielding an estimated size of approximately 33 nm. The calculated
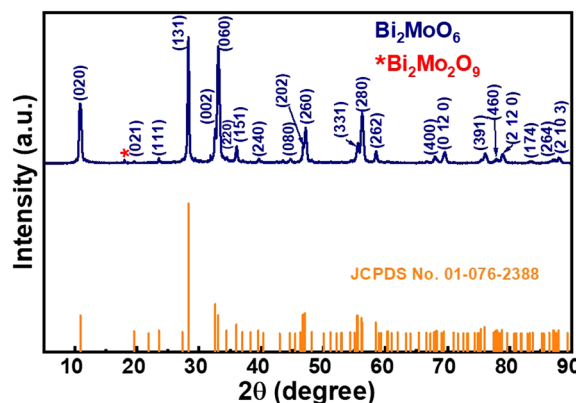

Fig. 2 XRD pattern of Bi$_2$MoO$_6$.

lattice parameters a, b, and c are 5.51 Å, 16.25 Å, and 5.47 Å, respectively, and are close to the reported literature.[14,15,23,37]

3.2. XPS analysis

Fig. S1 (ESI†) displays the full XPS survey spectrum of BMO, confirming the presence of Bi, Mo, O, C, and Na. In the magnified XPS spectra (Fig. 3(a)), peaks at 164.5 eV and 159.2 eV correspond to Bi $4f_{5/2}$ and Bi $4f_{7/2}$, respectively, indicating the presence of Bi^{3+}. Similarly, two peaks at 235.6 eV and 232.4 eV (Fig. 3(b)) are attributed to Mo $3d_{3/2}$ and Mo $3d_{5/2}$, confirming the presence of Mo^{6+}. The O 1s spectrum (Fig. 3(c)) shows two deconvoluted peaks at 530.2 eV and 532.4 eV, corresponding to Bi–O and Mo–O bonds, respectively.[14,21,22] The presence of these characteristic XPS peaks for Bi, Mo, and O confirms the formation of the Bi_2MoO_6 phase. Fig. 3(d) presents the C 1s spectrum, where deconvoluted peaks at 284.9 eV, 286.8 eV, and 288.8 eV correspond to C=C, C–O, and C=O bonds, respectively.[12,15] The detected carbon signal originates from the glacial acetic acid used during BMO synthesis. In addition, the Na 1s peak at 1072 eV (Fig. S2, ESI†) is attributed to the use of sodium molybdate as the Mo precursor.

3.3. Raman analysis

The Raman vibrational modes appear as bands at approximately 1047, 841, 795, 716, 400, 353, 325, 282, 200, 140, 94, and 59 cm^{-1}

(Fig. 4(a)). The band at 1047 cm^{-1} corresponds to the symmetric stretching modes of the NO_3^- anion.[40] The band at 841 cm^{-1} is attributed to the A_{2u} vibrational mode, indicating orthorhombic distortion in the MoO_6 octahedra, a characteristic feature of the Aurivillius Bi_2MoO_6 structure. The prominent signal at 795 cm^{-1} is associated with the A_{1g} mode, representing the symmetrical stretching of MoO_6 octahedra.[40,41] The peak at 716 cm^{-1} corresponds to the E_{1u} mode, linked to the asymmetric stretching of MoO_6 octahedra, involving the movement of equatorial oxygen atoms within the layers.[42,43] The modes at 400, 353, and 325 cm^{-1} correspond to E_{1u} bending vibrations, while the mode at 282 cm^{-1} is attributed to the E_9 bending vibration of the MoO_6 octahedra.[40,43–45] The lower-frequency modes at 200, 140, 94, and 59 cm^{-1} are associated with the translational movements of molybdenum and bismuth atoms. These results further confirm the successful synthesis of the Bi_2MoO_6 phase.[45–47]

3.4. FTIR analysis

The infrared spectrum of BMO is shown in Fig. 4(b). The vibrational band at approximately 582 cm^{-1} corresponds to the bending vibration of Mo–O, associated with the movement of equatorial oxygen atoms within the MoO_6 octahedra.[48] The absorption bands at 725 cm^{-1}, 793 cm^{-1}, and 840 cm^{-1} correspond to the asymmetric stretching vibration of equatorial oxygen atoms in MoO_6 octahedra, as well as the symmetric and
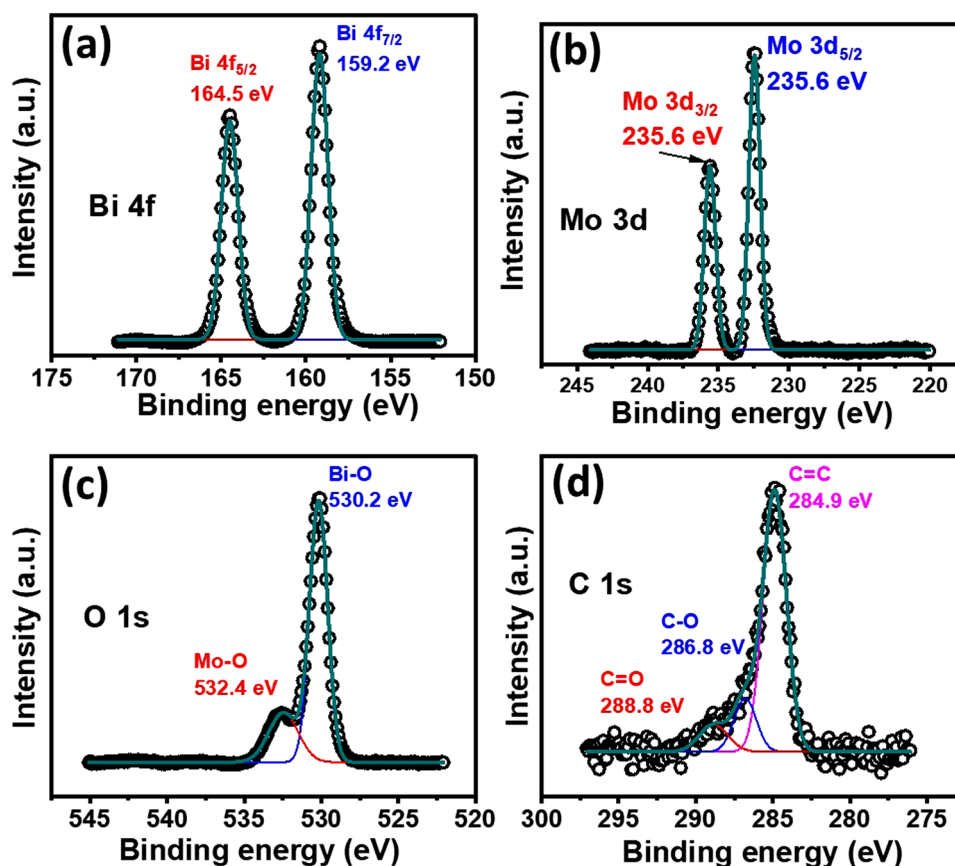

Fig. 3 XPS spectra of Bi_2MoO_6: (a) Bi 4f, (b) Mo 3d, (c) O 1s, and (d) C 1s.
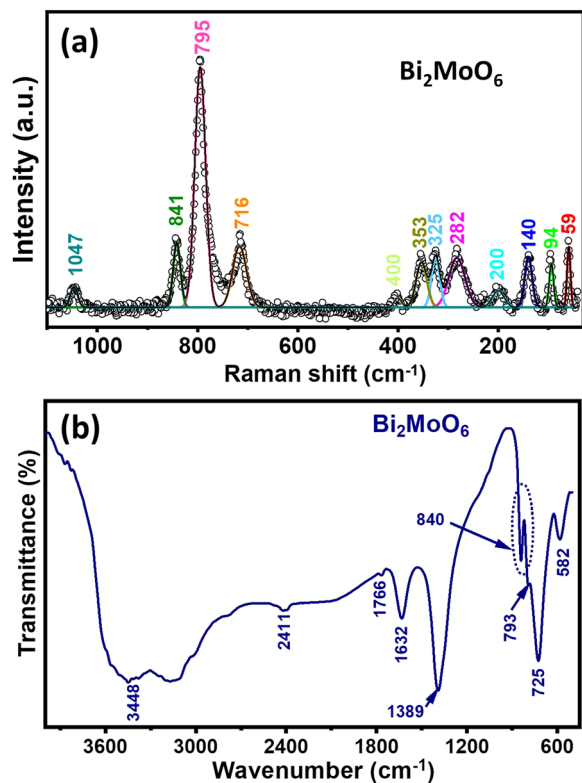
Fig. 4 (a) Raman spectra fitted to a Lorentzian type function, and (b) FTIR spectra of Bi_2MoO_6.

asymmetric stretching vibrations of apical oxygen atoms in the MoO_6 structure, respectively.[41,49,50] These characteristic bands confirm the successful formation of the Bi_2MoO_6 phase.

The absorption bands at 1632 cm^{-1} and 3448 cm^{-1} are attributed to the symmetric bending vibrations (in-plane scissoring) of the H–O–H bond and the O–H stretching vibration, respectively.[51] The peak at 2411 cm^{-1} is associated with CO_2, likely introduced from the atmosphere during sample preparation or handling.[51] Additionally, the absorption peak at 1389 cm^{-1} corresponds to the symmetric stretching vibration of the COO^- group, while the peak around 1766 cm^{-1} is attributed to the stretching vibration of the carbonyl group (C=O).[12,52] These peaks arise from the use of glacial acetic acid to dissolve bismuth nitrate during BMO synthesis, as further confirmed by the XPS results.

3.5. FESEM, EDS and elemental mapping analysis

Fig. 5(a) demonstrates the FESEM image of BMO, indicating the formation of a large number of random shaped nanoplates having the largest edge length between 200–700 nm and thickness 60–110 nm. The surfaces of these nanoplates are smooth. A similar kind of morphology was also reported previously for BMO.[53,54] Fig. 5(b) shows the EDS spectra of BMO and the inset highlights the experimentally determined atomic and weight percentages of each element present. The EDS spectra show prominent peaks for Bi, Mo, and O, along with traces of Na and
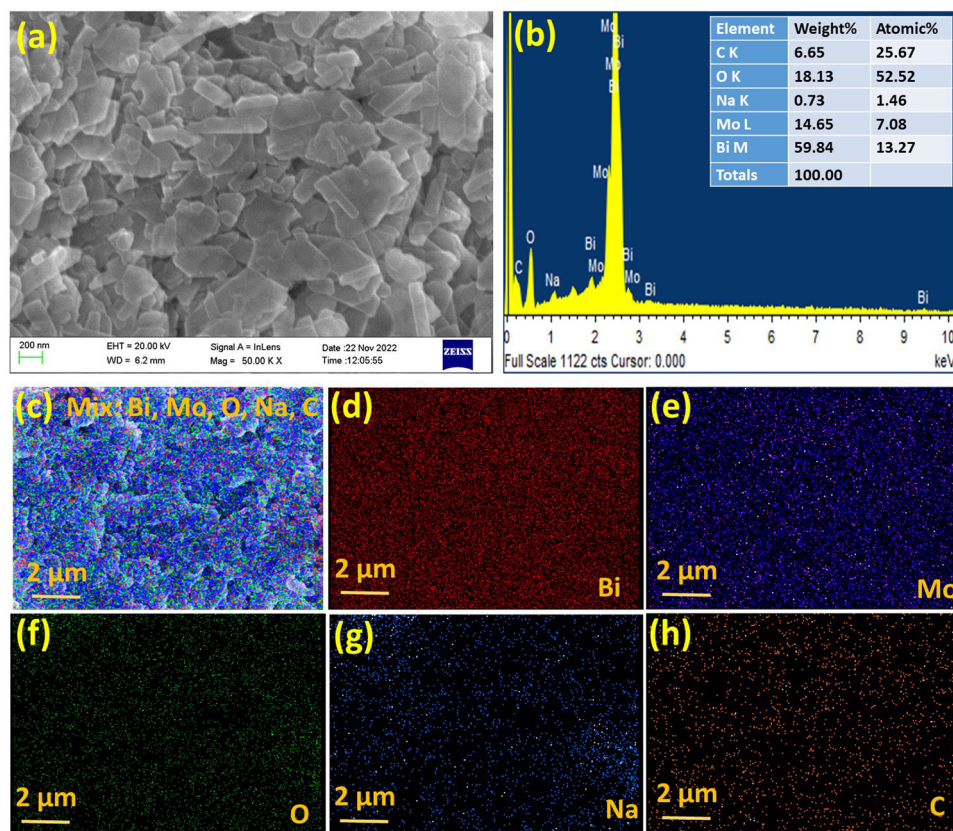

Fig. 5 (a) FESEM image, (b) EDS elemental composition, and (c)–(h) elemental mapping of BMO.

C, which are due to the precursor used during the synthesis of BMO. This result is consistent with XPS, and Raman results. The ratio of atomic percentage of Bi to Mo is approximately 1.87 : 1, which is close to the expected theoretical Bi to Mo atomic ratio 2 : 1. This indicates that the sample is prepared with the desired stoichiometry. Fig. 5(c) shows the mapping spectra for BMO. The mapping spectra (Fig. 5(d–h)) indicate that the elements are uniformly distributed throughout the sample.
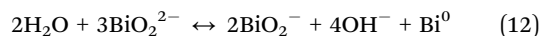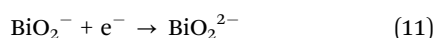
3.6. BET analysis

The nitrogen adsorption–desorption isotherm of BMO is shown in Fig. 6. The sample exhibits a BET surface area of approximately 50 m^2 g^{-1}. Additionally, the total pore volume of the BMO sample is 0.7567 cm^3 g^{-1}, with an estimated average pore diameter of around 60.5 nm.
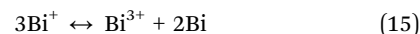
3.7. Electrochemical analysis

3.7.1. Three-electrode system. To evaluate the electrochemical performance of the BMO electrode, cyclic voltammetry (CV), galvanostatic charge–discharge (GCD), and electrochemical impedance spectroscopy (EIS) were conducted in a three-electrode setup using a 6 M KOH electrolyte.

Fig. 7(a) illustrates the CV curves of BMO at scan rates ranging from 10 to 100 mV s^{-1} in the potential range of −0.3 to 0.5 V (vs. Ag/AgCl). The CV profiles exhibit a pair of well-defined, quasi-reversible redox peaks, characteristic of typical battery-like (non-capacitive) behavior. These redox peaks indicate the electrochemical activity of the electrode, with the oxidation peak corresponding to the conversion of Bi metal to Bi(III), while the reduction peak represents the reverse process, where Bi(III) is reduced back to Bi metal. The redox reactions occurring during the electrochemical process can be represented by the following eqn (11)–(15):[12,13,15,18,21,26,55,56]

Reduction:

$$BiO_2^- + e^- \rightarrow BiO_2^{2-} \quad (11)$$

Fig. 6 N$_2$ adsorption–desorption isotherm of BMO (inset shows the BJH pore size distribution).

$$2H_2O + 3BiO_2^{2-} \leftrightarrow 2BiO_2^- + 4OH^- + Bi^0 \quad (12)$$

$$Bi^0 \rightarrow Bi \quad (13)$$

Oxidation:

$$Bi \rightarrow Bi^+ + e^- \quad (14)$$

$$3Bi^+ \leftrightarrow Bi^{3+} + 2Bi \quad (15)$$

The BMO exhibits excellent rate capability as an electrode material, as evidenced by the retention of its redox peaks even at a high scan rate of 100 mV s^{-1}. The specific capacity (C g^{-1}) is calculated at different scan rates (10–100 mV s^{-1}), as shown in Fig. 7(b). The BMO electrode exhibits the highest specific capacity of ∼229.18 mAh g^{-1} at 10 mV s^{-1}. Bi$_2$MoO$_6$ (BMO) demonstrates a high specific capacity primarily due to its unique electrochemical properties and structure, even though its surface area is moderate (∼50 m^2 g^{-1}) and the particle size is relatively large.

To further analyze the charge storage dynamics, the relationship between the peak current (i) and the scan rate (ν) is examined, with the b-value being calculated using eqn (16) and (17) as shown in Fig. 7(c):[57]

$$i = a\nu^b \quad (16)$$

$$\log(i) = \log(a) + b\log(\nu) \quad (17)$$

Typically, charge storage in electrode materials involves two reaction mechanisms: capacitive (surface-controlled) and diffusion-controlled processes. A b value close to 1 indicates a capacitive surface-controlled process, whereas a b value near 0.5 suggests a diffusion-controlled charge storage process. The estimated b value for BMO is approximately 0.53, indicating that diffusion-controlled charge storage dominates over the surface-controlled process. This dominance can be attributed to the intrinsic properties of BMO, where ion intercalation occurs within the bulk structure rather than being confined to surface adsorption. Consequently, this behavior classifies BMO as a battery-type material, where charge storage primarily depends on ion diffusion within its structure. The contribution percentages of both diffusion-controlled and capacitive surface-controlled reaction processes in the overall charge storage processes at different scan rates (10–100 mV s^{-1}) are shown in Fig. 7(d). They are calculated using the Dunn method[58] using eqn (18):

$$i = i_{capacitive} + i_{diffusive} = k_1\nu + k_2\nu^{1/2} \quad (18)$$

Here, ν is the scan rate (mV s^{-1}), and k_1 and k_2 are arbitrary constants. It is observed that the capacitive controlled contribution increases with increase in the scan rate. This is due to the fact that at higher scan rate, the electrolytic ions do not get sufficient time to interact deep within the electrode material. They are able to interact with the electrode material at the surface only and hence, contribute to the charge storage via the formation of an electric double layer of charges at the interface of the electrode and electrolyte. This leads to increased capacitive controlled contribution at higher scan rates.[57] However,
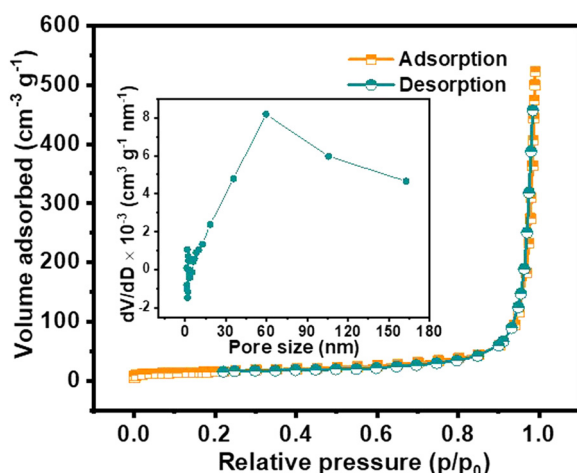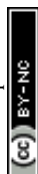
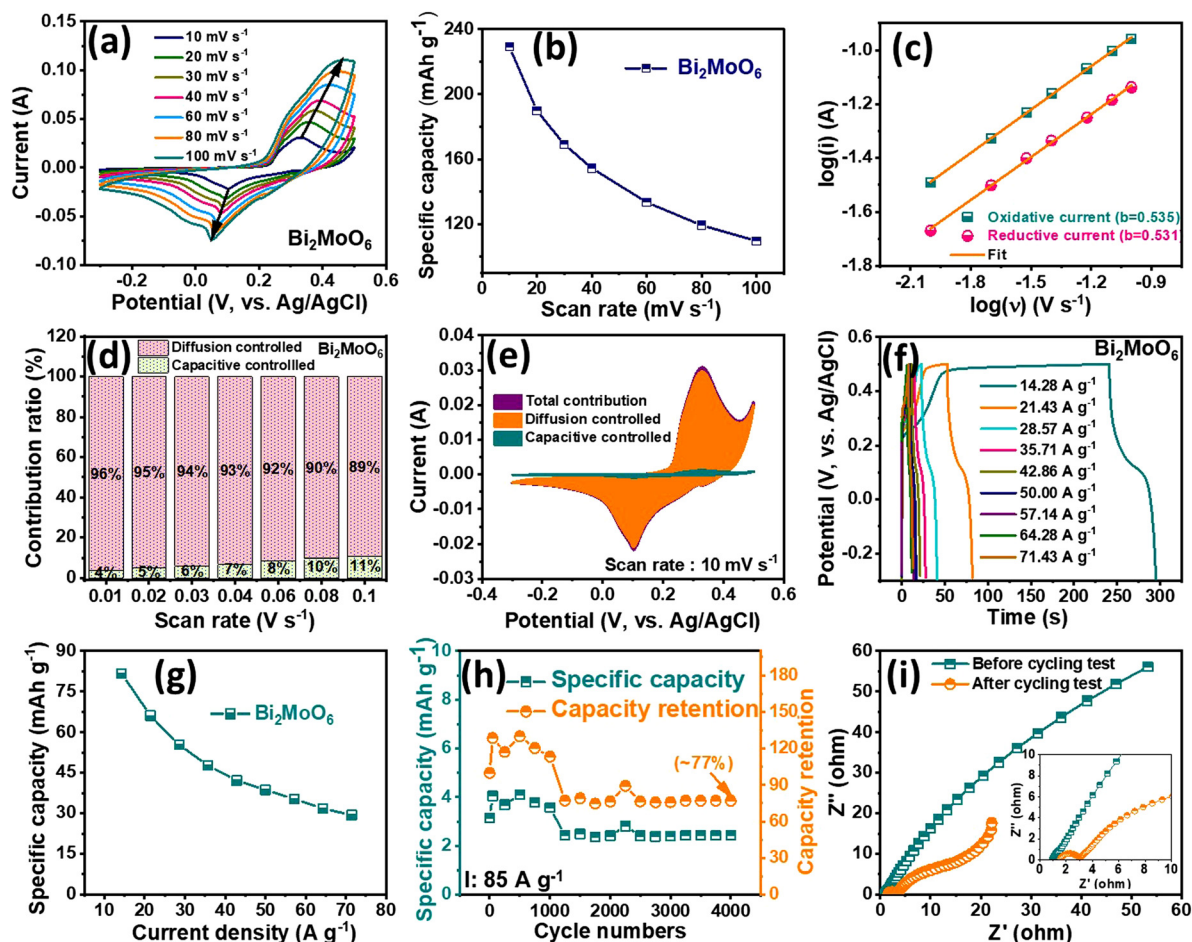© 2025 The Author(s). Published by the Royal Society of Chemistry

Fig. 7 (a) CV curves at various scan rates, (b) specific capacity *versus* scan rate, (c) log(i) *versus* log(ν), (d) capacitive and diffusion charge contribution at different scan rates, (e) CV curve demonstrating the capacitive and diffusive contribution at 10 mV s^{-1}, (f) GCD curves at different current densities, (g) specific capacity *versus* current densities, (h) durability test, and (i) EIS plots before and after the durability test of the BMO electrode.

as the scan rate is decreased, the electrolytic ions get sufficient time to penetrate deep inside the electrode material and participate significantly in the faradaic redox reactions with the electrode material. Thus, the diffusive controlled contribution of charges increases at lower scan rate. The dominance of the diffusion-controlled reaction process at lower scan rate indicates the battery-kind charge storage mechanism in the BMO sample and signifies BMO as a battery-kind material. Fig. 7(e) shows the CV curve of the BMO electrode at a scan rate of 10 mV s^{-1}, further illustrating the contributions of both capacitive and diffusive processes. Thus, BMO operates through a faradaic process involving redox reactions and ion intercalation and the high faradaic redox activity of bismuth (Bi^{3+}/Bi^0) in combination with molybdate ions contributes to a diffusion-controlled charge storage process, enabling a greater specific capacity and higher charge retention over time. The layered structure of BMO facilitates efficient ion diffusion and electron transport and this structural feature compensates for the moderate surface area and larger particle size by enabling deep penetration of ions into the BMO, enhancing its electrochemical performance. In addition, BMO combines both

battery-like faradaic and supercapacitor-like capacitive charge storage (hybrid mechanism), allowing it to deliver a balance of high energy and power density, as both the bulk and surface contribute to the overall charge storage process.

Fig. 7(f) presents the typical GCD curves of the BMO electrode at various current densities ranging from 14.28 to 71.43 A g^{-1} within a voltage window of −0.3 to 0.5 V. The discharge voltage plateaus observed in the GCD curves align well with the CV curves. The specific capacity (C_m) is determined from the discharge curves at different current densities, as shown in Fig. 7(g). The highest capacity of approximately 82 mAh g^{-1} is achieved at a current density of 14.28 A g^{-1}, retaining 16.22 mAh g^{-1} even at 71.43 A g^{-1}, demonstrating the BMO electrode's substantial capacity retention with increasing current density.

Fig. 7(h) illustrates the cycling stability of BMO electrodes at a high current density of 85 A g^{-1} over 4000 cycles for real-time applications. Notably, the BMO electrode exhibits excellent long-term stability, maintaining approximately 77% of its initial capacity (coulombic efficiency ∼58%) at the end of the durability test, attributed to its robust structural integrity. However, the
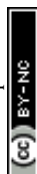
slight decline in capacity over 4000 cycles may be linked to structural strain induced by repeated charge/discharge cycles, which can affect the integrity of the active material. In order to investigate the effect of repeated charging and discharging on the structure of BMO, the XRD of the BMO electrode after the cyclic stability test for 4000 charge/discharge cycles has been carried out and is provided in Fig. S5 in the ESI.† After the stability test, the XRD pattern of BMO shows a few additional peaks at (002) and (222), marked with # in Fig. S5 (ESI†) corresponding to the bismuth oxide phase, along with the characteristic peaks of BMO.[14] During long-term electrochemical cycling, the repeated faradaic redox reactions ($Bi^{3+} \rightleftharpoons Bi^0$) can lead to structural strain and localized breakdown of the BMO lattice. This mechanical and chemical stress may disrupt the original Bi_2MoO_6 framework, causing bismuth to segregate or re-oxidize, resulting in the formation of secondary bismuth oxide phases.[15,18,56] In addition, the alkaline environment (6 M KOH) used as the electrolyte can enhance surface dissolution or leaching of Mo species, destabilizing the MoO_6 layers and promoting the formation of Bi-rich oxide phases like Bi_2O_3.[18,38] Compared to previous studies on BMO-based supercapacitor devices,[24,26,27,59–62] these results highlight enhanced stability and high-rate performance.

Many previously reported BMO materials show lower retention at high current densities due to more rapid degradation of their crystal structure. This work thus highlights the advantage of our synthesis approach, yielding a BMO structure that maintains a commendable balance between energy and power density under demanding cycling conditions, advancing its applicability in high-performance energy storage solutions. Fig. 7(i) illustrates the EIS curves obtained for the BMO electrode before and after conducting the stability test. The R_s and R_{ct} values are 0.94 and 0.84 Ω, respectively, for the EIS curve before the durability test. Similarly, the R_s and R_{ct} values are 1.5 and 1.55 Ω, respectively, for the EIS curve obtained after the durability test. The small increase in resistance values indicates that the BMO electrode experiences minimal degradation in terms of charge-transfer resistance, further supporting its excellent long-term electrochemical performance.

3.7.2. Two-electrode system. To evaluate the capacitive performance of the BMO electrode for practical applications, it was tested separately in symmetric (BMO//BMO) and asymmetric (BMO//CNTs) supercapattery configurations. The potential windows were optimized for both setups, as shown in Fig. S3 (ESI†). In the ASC (BMO//CNT) configuration, where BMO serves as the positive electrode and CNT as the negative electrode, individual CV curves for both electrodes were obtained from a three-electrode measurement system. The optimized working potential windows were 0 to 0.5 V for the BMO electrode and −1 to 0 V for the CNT electrode, measured at a scan rate of 10 mV s⁻¹ (Fig. S4, ESI†).

Fig. 8(a and b) presents the CV curves of the BMO//BMO and BMO//CNT devices at different scan rates (10–100 mV s⁻¹) within their optimized stable voltage windows of 1.5 V and 1.4 V, respectively. Both configurations exhibit distinct redox peaks corresponding to the $Bi^{3+} \rightleftharpoons Bi^0$ redox transition, even at

a high scan rate of 100 mV s⁻¹, indicating a strong rate capability, consistent with the single-electrode testing results. The specific capacity (mAh g⁻¹) for both devices, calculated from their CV curves at different scan rates, is shown in Fig. 8(c). The highest specific capacity values recorded were ∼70.56 mAh g⁻¹ for the BMO//BMO device and 58.06 mAh g⁻¹ for the BMO//CNT device at 10 mV s⁻¹.

Notably, the BMO electrode exhibits a higher specific capacity in the symmetric configuration compared to the asymmetric one. This enhancement in the BMO//BMO device is attributed to the presence of redox-active BMO as both the anode and cathode material, facilitating a symmetrical charge storage mechanism where similar intercalation and redox processes occur at both electrodes. The full utilization of redox activity, deeper ion penetration, and balanced faradaic contributions contribute to the higher capacity in the symmetric configuration. In the asymmetric BMO//CNT setup, the BMO electrode functions as the positive electrode, while the CNT electrode primarily stores charge through non-faradaic capacitive processes. Since the CNT electrode does not participate in redox reactions, the total charge storage primarily relies on the BMO electrode, limiting the overall capacity compared to the symmetric configuration. While the CNT electrode enhances conductivity and reduces ion diffusion resistance, it does not directly contribute to increased specific capacity, as charge storage is mainly determined by the redox-active BMO electrode in the asymmetric setup. Furthermore, GCD tests for both BMO//BMO and BMO//CNT devices were conducted within an optimized voltage window of 1.4 V across a range of current densities (0.71–5.0 A g⁻¹), as shown in Fig. 8(d and e). The IR drop (∼0.4 V) observed in the GCD plot of Bi_2MoO_6 is due to its low electronic conductivity and the internal resistance of the active electrode material, which hinders the efficient transport of electrons during charge transfer. In addition, the presence of resistive interfaces between the Bi_2MoO_6 material and the current collector, or within the material itself, can also contribute to the observed IR drop.[15,22,24,31] The specific capacity values, calculated from the GCD curves at different current densities, are summarized in Fig. 8(f). The specific capacity of BMO//BMO is higher compared to BMO//CNT at current densities ranging from 0.71–2.86 A g⁻¹, while the value of specific capacity is almost equal at higher current densities (3.57–5.0 A g⁻¹).

The highest specific capacity for the BMO//BMO and BMO//CNT devices is ∼83 mAh g⁻¹ and ∼46.25 mAh g⁻¹, respectively at 0.71 A g⁻¹, which is decreased to ∼27.15 mAh g⁻¹, and ∼28.60 mAh g⁻¹ at 5.0 A g⁻¹, which shows better capacity retention with an increase in current density in BMO//CNT (∼62%) compared to the BMO//BMO (∼32.65%) device configuration. The observed differences in rate capability arise from distinct characteristics in each configuration. In the BMO//CNT device, the CNT electrode's high conductivity promotes efficient charge transport, minimizing ion diffusion and charge transfer resistance. This results in a more stable performance and greater capacity retention across various current densities. Conversely, the BMO//BMO device shows
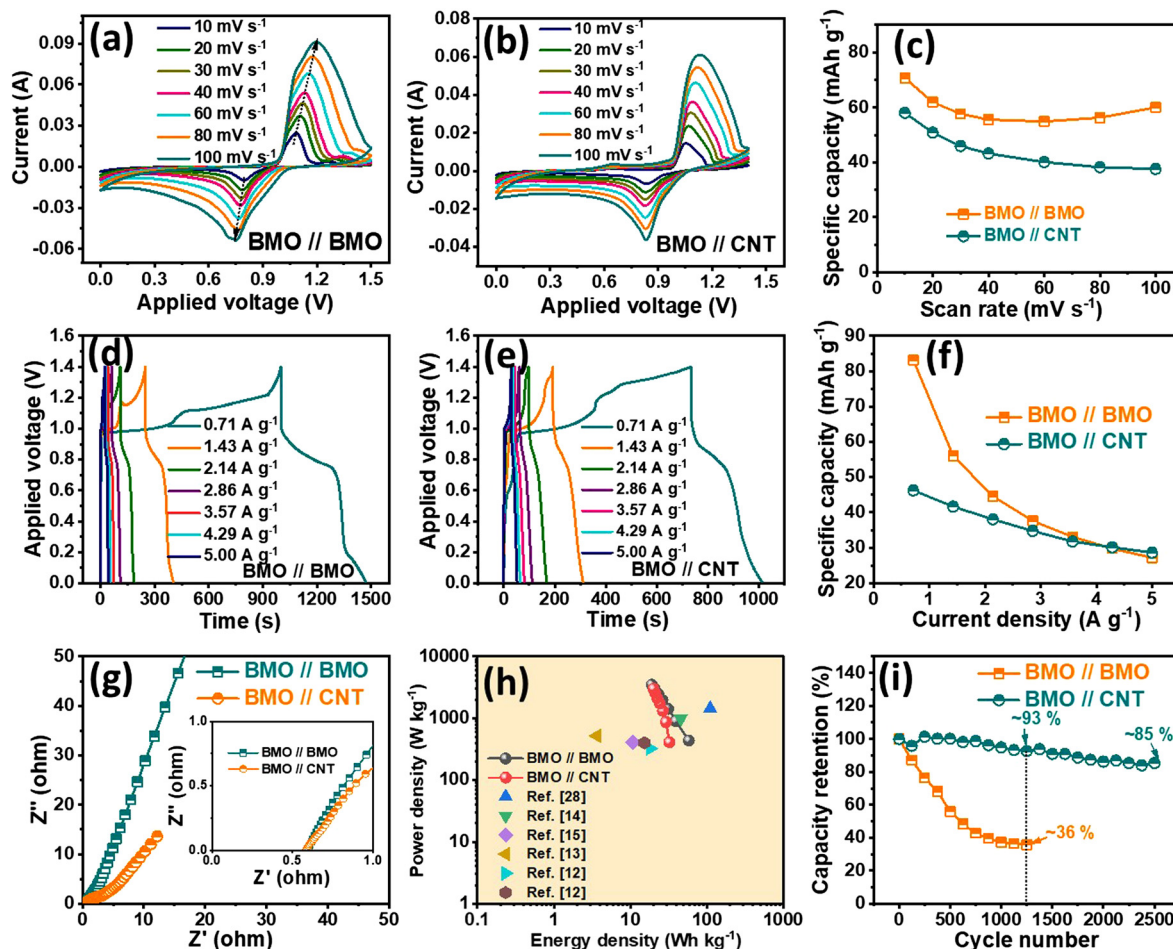
Fig. 8 (a) and (b) CV curves at various scan rates, (c) specific capacity *versus* scan rate, (d) and (e) GCD curves at different current densities, (f) specific capacity *versus* current densities, (g) EIS plots, (h) energy density *versus* power density, and (i) durability test of the BMO//BMO and BMO//CNT cell.

Table 1 Summary of electrochemical performance of Aurivillius electrode materials for supercapattery device design

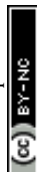| Electrode	Electrolyte	Specific capacity	Potential window of GCD (V)	Energy density (Wh kg^{-1})	Power density (W kg^{-1})	Capacity retention % (cycles)	Ref.
Au@Bi$_2$O$_3$/Bi$_2$WO$_6$// Au@Bi$_2$O$_3$/Bi$_2$WO$_6$	6 M KOH	5.05 F g^{-1} at 0.2 A g^{-1}	−0.3 to 0.9	3.636	521.66	—	13
Bi$_4$Ti$_3$O$_{12}$@CNF// Bi$_4$Ti$_3$O$_{12}$@CNF CNF-carbon nanofiber	6 M KOH	25.85 mAh g^{-1} at 0.5 A g^{-1}	0–1.4	18.09	325.39	66% (7000)	12
Bi$_4$Ti$_3$O$_{12}$@CNF//CNF	6 M KOH	20.38 mAh g^{-1} at 0.5 A g^{-1}	0–1.4	15.29	403.74	63% (3500)	12
(MBiN/ACC)//(MBiN/ACC) mesoporous Bi$_2$MoO$_6$–MBiN activated carbon cloth-ACC	PVA-KOH gel electrolyte	345.0 F g^{-1} at 1 A g^{-1}	0–0.8	110.4	1429.6	90.2% (10 000)	18
Bi$_2$MoO$_6$//Bi$_2$MoO$_6$	1 M KOH polypropylene separator	40.5 F g^{-1} at 1 A g^{-1}	0–1.5	45.6	989	78% 5000	14
CS@ Bi$_2$MoO$_6$//CS@Bi$_2$MoO$_6$ carbon spheres-CS	PVA–KOH thin film	26.69 F g^{-1} at 0.25 A g^{-1}	0–0.9	10.8	410	78.90% (10 000)	15
Bi$_2$MoO$_6$//CNT	6 M KOH	46.25 mAh g^{-1} at 0.7 A g^{-1}	0–1.4	32.38	410.62	85% (2500)	This work
Bi$_2$MoO$_6$//Bi$_2$MoO$_6$	6 M KOH	83.12 mAh g^{-1} at 0.7 A g^{-1}	0–1.4	58.19	439.18	36% (1250)	This work
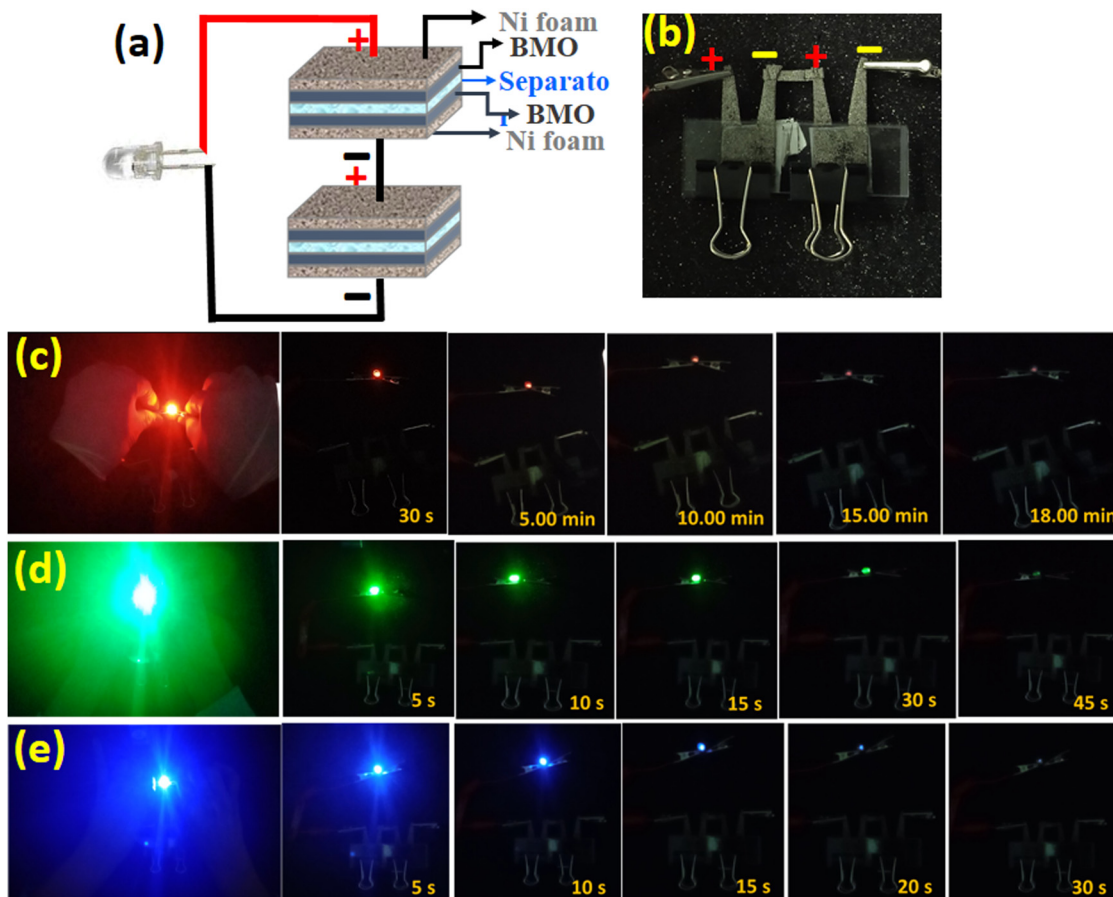
Fig. 9 (a) and (b) Schematic and photographic images of the series connection of two symmetric supercapatteries and (c) and (e) real-time feasibility of the supercapattery tested by energizing red, green, and blue LEDs.

high initial capacity at low current densities, as charge carriers penetrate deeply into the bulk of the BMO, fully engaging its redox-active sites. However, as current density increases, the BMO//BMO configuration becomes surface-limited, with the ions primarily interacting at the surface rather than within the bulk.[4,63] This surface-restricted charge storage at high currents, combined with the absence of a conductive additive CNT, limits the BMO//BMO device's rate capability compared to BMO//CNT. The EIS study of both device configurations has been undertaken, and the corresponding Nyquist plots are shown in Fig. 8(g). The R_s value for BMO//BMO and BMO//CNT is 0.56 and 0.6 Ω, respectively, while the charge transfer and ion diffusion resistance are lower in BMO//CNT than in the BMO//BMO device configuration. This enhanced conductivity in the BMO//CNT device facilitates more efficient charge transport, contributing to better rate capability, as observed in the GCD tests. The energy and power densities for both device configurations were calculated and plotted in the Ragone plot (Fig. 8(h)) and compared with the results from other recently reported Aurivillius compounds, as summarized in Table 1. The highest energy density of BMO//BMO is 58.19 Wh kg^{-1} (with a power density of 439.18 W kg^{-1}), which decreases to 19 Wh kg^{-1} (with a power density of 3485 W kg^{-1}). In comparison, BMO//CNT shows the highest energy density of 32.38 Wh kg^{-1}

(with a power density of 410.62 W kg^{-1}), which decreases to 20 Wh kg^{-1} (with a power density of 3009 W kg^{-1}). Furthermore, a charge/discharge cycling test was carried out to evaluate the cycling stability of both the fabricated devices, as shown in Fig. 8(i). The capacity retention is 36% for BMO//BMO after 1250 cycles, while BMO//CNT shows better capacity retention of 85% after 2500 cycles. The higher capacity retention in the asymmetric BMO//CNT configuration can be attributed to the fact that CNTs can provide good electrical conductivity and mechanical stability to the device, which can prevent the degradation of the active material BMO on the anode side during cycling.[64] Furthermore, to assess the practicality of the device, LED tests are conducted after connecting two identical SC cells in series. The resulting device is capable of illuminating red, green and blue LEDs for ~18 minutes, 45 s, and 30 s, respectively (see Fig. 9).

4. Conclusion

This study demonstrates that Bi$_2$MoO$_6$ synthesized *via* a microwave-assisted hydrothermal methods excels in both symmetric (BMO//BMO) and asymmetric (BMO/CNT) supercapattery configurations. The symmetric device delivers higher specific

capacity, while the asymmetric configuration offers enhanced retention and rate capability. The higher specific capacity of the BMO//BMO device is due to the redox-active BMO at both electrodes, enabling symmetrical intercalation and redox processes with deeper ion penetration and balanced faradaic contribution. In contrast, the BMO//CNT device relies mainly on the BMO electrode for charge storage, as the CNT electrode only provides non-faradaic capacitance. Although CNT enhances conductivity and reduces ion diffusion resistance, it does not increase specific capacity since the redox activity is limited to the BMO electrode. However, the conductive properties of the CNT electrode facilitate more efficient charge transport and enhance the rate capability in the asymmetric device. Additionally, the symmetric supercapattery device is able to successfully illuminate different colored LEDs for varying durations. Compared to previously reported BMO-based materials, the results from this study represent a significant improvement in both electrochemical performance and stability, making BMO a promising candidate for high-performance next-generation energy storage devices.

Author contributions

Anu: conceptualization, methodology, visualization, investigation, validation, writing of original draft, review and editing. Khadim Hussain, Prakash Chand, J. Nagendra Babu, and C.S. Yadav: investigation, validation, review and editing. Joel Garcia: visualization, investigation, validation, review and editing. Surender Kumar Sharma, and Kamlesh Yadav: supervision, visualization, investigation, validation, review and editing.

Conflicts of interest

There are no conflicts to declare.

Data availability

Data will be available on request.

Acknowledgements

References

1 L. Yu and G. Z. Chen, Supercapatteries as High-Performance Electrochemical Energy Storage Devices, *Electrochem. Energy Rev.*, 2020, **3**(2), 271–285.

2 G. Z. Chen, Linear and non-linear pseudocapacitances with or without diffusion control, *Prog. Nat. Sci.: Mater. Int.*, 2021, **31**(6), 792–800.

3 G. Z. Chen, Supercapattery: Merit merge of capacitive and Nernstian charge storage mechanisms. Current Opinion in, *Electrochemistry*, 2020, **21**, 358–367.

4 L. Yu and G. Z. Chen, Redox electrode materials for supercapatteries, *J. Power Sources*, 2016, **326**, 604–612.

5 V. Sankar Devi, *et al.*, Facile sol-gel derived nanostructured spinel Co_3O_4 as electrode material for high-performance supercapattery and lithium-ion storage, *J. Energy Storage*, 2019, **25**, 100815.

6 I. Heng, *et al.*, High performance supercapattery with rGO/TiO_2 nanocomposites anode and activated carbon cathode, *J. Alloys Compd.*, 2019, **796**, 13–24.

7 P. M. Junais, *et al.*, Supercapattery performances of nanostructured cerium oxide synthesized using polymer soft-template, *J. Energy Storage*, 2020, **28**, 101241.

8 N. M. Shinde, *et al.*, Ultra-rapid chemical synthesis of mesoporous Bi_2O_3 micro-sponge-balls for supercapattery applications, *Electrochim. Acta*, 2019, **296**, 308–316.

9 M. P. Harikrishnan, A. J. C. Mary and A. C. Bose, Electrochemical performance of $ANiO_3$ (A = La, Ce) perovskite oxide material and its device performance for supercapattery application, *Electrochim. Acta*, 2020, **362**, 137095.

10 A. K. Nayak and T. Gopalakrishnan, Phase- and Crystal Structure-Controlled Synthesis of Bi_2O_3, Fe_2O_3, and $BiFeO_3$ Nanomaterials for Energy Storage Devices, *ACS Appl. Nano Mater.*, 2022, **5**(10), 14663–14676.

11 B. Saravanakumar, *et al.*, Holey two dimensional manganese cobalt oxide nanosheets as a high-performance electrode for supercapattery, *Chem. Eng. J.*, 2019, **373**, 547–555.

12 Anu, *et al.*, Unleashing supercapattery potential with microwave-engineered bismuth titanate ($Bi_4Ti_3O_{12}$)/carbon nanofiber (CNF) composites, *J. Energy Storage*, 2024, **89**, 111646.

13 G. H. Gote, *et al.*, Development of pristine and Au-decorated Bi_2O_3/Bi_2WO_6 nanocomposites for supercapacitor electrodes, *RSC Adv.*, 2019, **9**(56), 32573–32580.

14 P. V. Shinde, *et al.*, Facile Chemical Synthesis and Potential Supercapattery Energy Storage Application of Hydrangea-type Bi_2MoO_6, *ACS Omega*, 2019, **4**(6), 11093–11102.

15 K. J. Samdani, *et al.*, Self-Assembled Bi_2MoO_6 Nanopetal Array on Carbon Spheres toward Enhanced Supercapacitor Performance, *ACS Sustainable Chem. Eng.*, 2018, **6**(12), 16702–16712.

16 M. Z. Iqbal and U. Aziz, Supercapattery: Merging of battery-supercapacitor electrodes for hybrid energy storage devices, *J. Energy Storage*, 2022, **46**, 103823.

17 V. D. Nithya, *et al.*, Surfactant assisted sonochemical synthesis of Bi_2WO_6 nanoparticles and their improved electrochemical properties for use in pseudocapacitors, *RSC Adv.*, 2014, **4**(9), 4343–4352.

18 L. Wang, *et al.*, Mesoporous Bi_2MoO_6 quasi-nanospheres anchored on activated carbon cloth for flexible all-solid-state supercapacitors with enhanced energy density, *J. Power Sources*, 2020, **463**, 228202.

19 M. Lyu, *et al.*, Advances in modification of Bi_2MoO_6 and its photocatalysis: A review, *J. Alloys Compd.*, 2024, **982**, 173759.

20 Z. Xie, et al., Enhancing photoelectrochemical performance of the Bi_2MoO_6 photoanode by ferroelectric polarization regulation, Nanoscale, 2020, **12**(35), 18446–18454.

21 T. Yu, et al., Facile Synthesis of Flowerlike Bi_2MoO_6 Hollow Microspheres for High-Performance Supercapacitors, ACS Sustainable Chem. Eng., 2018, **6**(6), 7355–7361.

22 Z.-Q. Liu, et al., Facile Synthesis of Large-Area Hierarchical Bismuth Molybdate Nanowires for Supercapacitor Applications, J. Electrochem. Soc., 2012, **159**(10), D582.

23 B. Senthilkumar, et al., Synthesis, crystal structure and pseudocapacitor electrode properties of γ-Bi_2MoO_6 nanoplates, Solid State Sci., 2014, **35**, 18–27.

24 X. Yu, et al., Rose-like Bi_2MoO_6 microsphere as electrode material for high performance supercapacitor, Int. J. Electrochem. Sci., 2019, **14**(6), 5629–5636.

25 J. Yesuraj, S. A. Suthanthiraraj and O. Padmaraj, Synthesis, characterization and electrochemical performance of DNA-templated Bi_2MoO_6 nanoplates for supercapacitor applications, Mater. Sci. Semicond. Process., 2019, **90**, 225–235.

26 S. K. Hussain, B. Dudem and J. S. Yu, Enhanced electrochemical performance via PPy encapsulated 3D flower-like bismuth molybdate nanoplates for high-performance supercapacitors, Appl. Surf. Sci., 2019, **478**, 846–856.

27 F. Wu, et al., Synthesis and characterization of hierarchical Bi_2MoO_6/Polyaniline nanocomposite for all-solid-state asymmetric supercapacitor, Electrochim. Acta, 2017, **245**, 685–695.

28 J. Yesuraj and S. A. Suthanthiraraj, DNA-mediated sonochemical synthesis and characterization of octahedron-like bismuth molybdate as an active electrode material for supercapacitors, J. Mater. Sci.: Mater. Electron., 2018, **29**(7), 5862–5872.

29 K. R. Kendall, et al., Recent Developments in Oxide Ion Conductors: Aurivillius Phases, Chem. Mater., 1996, **8**(3), 642–649.

30 D. Zhu, et al., Time-dependent evolution of the dichloromethane-mediated Bi_2MoO_6/BiOCl heterojunction for enhanced electrochemical performance, J. Solid State Electrochem., 2017, **21**(10), 2955–2964.

31 A. Shameem, et al., Robust one-step synthesis of bismuth molybdate nanocomposites: A promising negative electrode for high end ultracapacitors, Solid State Sci., 2020, **106**, 106303.

32 T. A. Hanna, The role of bismuth in the SOHIO process, Coord. Chem. Rev., 2004, **248**(5), 429–440.

33 Y. Deng, et al., Yolk–Shell Structured Nickel Cobalt Sulfide and Carbon Nanotube Composite for High-Performance Hybrid Supercapacitors, Energy Fuels, 2021, **35**(6), 5342–5351.

34 S. C. Sekhar, et al., Nanosilver-Particles Integrated $Ni_3Sn_2S_2$-CoS Composite as an Advanced Electrode for High Energy Density Hybrid Cell, Small Methods, 2021, **5**(12), 2100907.

35 M. F. L. De Volder, et al., Carbon Nanotubes: Present and Future Commercial Applications, Science, 2013, **339**(6119), 535–539.

36 S. Zhu, J. Ni and Y. Li, Carbon nanotube-based electrodes for flexible supercapacitors, Nano Res., 2020, **13**(7), 1825–1841.

37 D. Wang, et al., Porous $BiOBr$/Bi_2MoO_6 Heterostructures for Highly Selective Adsorption of Methylene Blue, ACS Omega, 2016, **1**(4), 566–577.

38 S. Baduri, et al., Optimization of semiconductor–electrolyte interfacial phenomena for stable and efficient photoelectrochemical water oxidation behavior of $Bi_2Mo_2O_9$–Bi_2MoO_6 heterojunction, Electrochim. Acta, 2021, **372**, 137754.

39 U. Holzwarth and N. Gibson, The Scherrer equation versus the 'Debye-Scherrer equation', Nat. Nanotechnol., 2011, **6**(9), 534.

40 C. Kongmark, et al., Synthesis of γ-Bi_2MoO_6 catalyst studied by combined high-resolution powder diffraction, XANES and Raman spectroscopy, Catal. Today, 2010, **157**(1), 257–262.

41 M. Shetty, et al., One-pot supercritical water synthesis of Bi_2MoO_6-RGO 2D heterostructure as anodes for Li-ion batteries, Ceram. Int., 2021, **47**(7, Part B), 10274–10283.

42 A. Phuruangrat, et al., Hydrothermal synthesis, structure, and optical properties of pure and silver-doped Bi_2MoO_6 nanoplates, Russ. J. Phys. Chem. A, 2015, **89**(13), 2443–2448.

43 H. Li, et al., Enhancement of photocatalytic activity in Tb/Eu co-doped Bi_2MoO_6: the synergistic effect of Tb–Eu redox cycles, RSC Adv., 2016, **6**(53), 48089–48098.

44 L. Zhang, et al., Controllable synthesis of Bi_2MoO_6 and effect of morphology and variation in local structure on photocatalytic activities, Appl. Catal., B, 2010, **98**(3), 138–146.

45 J. Yesuraj, S. Austin Suthanthiraraj and O. Padmaraj, Synthesis, characterization and electrochemical performance of DNA-templated Bi_2MoO_6 nanoplates for supercapacitor applications, Mater. Sci. Semicond. Process., 2019, **90**, 225–235.

46 R. Wang, et al., Preparation, Characterization, and Performance Analysis of S-Doped Bi_2MoO_6 Nanosheets, Nanomaterials, 2019, **9**(9), 1341.

47 A. Phuruangrat, et al., Hydrothermal Synthesis of Bi_2MoO_6 Visible-Light-Driven Photocatalyst, J. Nanomater., 2015, **2015**(1), 135735.

48 A. Phuruangrat, et al., Synthesis and characterization of visible-light-driven Cl-doped Bi_2MoO_6 photocatalyst with enhanced photocatalytic activity, Mater. Lett., 2017, **196**, 256–259.

49 D. Tang, et al., Enhanced Photoelectrochemical Performance of Porous Bi_2MoO_6 Photoanode by an Electrochemical Treatment, J. Electrochem. Soc., 2017, **164**(6), H299.

50 J. Guo, et al., Synthesis and Characterization of $SrFeO_{2.73}$/Bi_2MoO_6 Heterojunction with Enhanced Photocatalytic Activity, Catal. Lett., 2021, **151**(8), 2176–2186.

51 Anu, et al., Effect of oxygen vacancies, lattice distortions and secondary phase on the structural, optical, dielectric and ferroelectric properties in Cd-doped $Bi_2Ti_2O_7$ nanoparticles., Mater. Res. Bull., 2021, **141**, 111373.

52 M. T. Colomer, Straightforward synthesis of Ti-doped YSZ gels by chemical modification of the precursors alkoxides, J. Sol-Gel Sci. Technol., 2013, **67**(1), 135–144.

53 A. Phuruangrat, et al., Hydrothermal synthesis, characterization, and optical properties of Ce doped Bi_2MoO_6 nanoplates, J. Nanomater., 2014, **2014**, Article 7.

54 S. Maswanganyi, *et al.*, Bismuth Molybdate Nanoplates Supported on Reduced Graphene Oxide: An Effective Nano-composite for the Removal of Naphthalene via Adsorption–Photodegradation, *ACS Omega*, 2021, **6**(26), 16783–16794.

55 B. Sarma, *et al.*, Redox-Induced Enhancement in Interfacial Capacitance of the Titania Nanotube/Bismuth Oxide Composite Electrode, *ACS Appl. Mater. Interfaces*, 2013, **5**(5), 1688–1697.

56 V. Vivier, *et al.*, Electrochemical Study of Bi_2O_3 and $Bi_2O_2CO_3$ by Means of a Cavity Microelectrode. I. Observed Phenomena and Direct Analysis of Results, *J. Electrochem. Soc.*, 2000, **147**(11), 4252.

57 R. Kumar and M. Bag, Quantifying Capacitive and Diffusion-Controlled Charge Storage from 3D Bulk to 2D Layered Halide Perovskite-Based Porous Electrodes for Efficient Supercapacitor Applications. The, *J. Phys. Chem. C*, 2021, **125**(31), 16946–16954.

58 J. Wang, *et al.*, Pseudocapacitive Contributions to Electrochemical Energy Storage in TiO_2 (Anatase) Nanoparticles. The, *J. Phys. Chem. C*, 2007, **111**(40), 14925–14931.

59 Y. Ma, *et al.*, Facile growth of Bi_2MoO_6 nanosheet arrays on Ni foam as an electrode for electrochemical applications, *RSC Adv.*, 2016, **6**(15), 12093–12099.

60 Y. Ma, *et al.*, Hierarchical nanosheet-based Bi_2MoO_6 nanotubes with remarkably improved electrochemical performance, *J. Power Sources*, 2016, **331**, 481–486.

61 Y. Jia, *et al.*, Hierarchical $NiCo_2O_4$/Bi_2MoO_6 heterostructured nanorod arrays for high-performance supercapacitors, *Mater. Lett.*, 2019, **244**, 130–133.

62 J. Wen, *et al.*, Facile synthesis of a Bi_2MoO_6/TiO_2 nanotube arrays composite by the solvothermal method and its application for high-performance supercapacitor, *RSC Adv.*, 2019, **9**(9), 4693–4699.

63 Y. Gogotsi and R. M. Penner, *Energy storage in nanomaterials–capacitive, pseudocapacitive, or battery-like?*, 2018, ACS Publications, pp. 2081–2083.

64 H. Pan, J. Li and Y. Feng, Carbon Nanotubes for Supercapacitor, *Nanoscale Res. Lett.*, 2010, **5**(3), 654.